Original research article

Three-dimensional semiautomatic liver segmentation method for non-contrast computed tomography based on a correlation map of locoregional histogram and probabilistic atlas

Satoshi Yamaguchi[a, *], Koji Satake[b], Yoshio Yamaji[b], Hiromi T. Tanaka[b]

[a] Department of Biomaterials Science, Osaka University Graduate School of Dentistry, 1-8 Yamadaoka, Suita, Osaka 565-0871, Japan

[b] College of Information Science and Engineering, Ritsumeikan University, 1-1-1 Nojihigashi, Kusatsu, Shiga 525-8577, Japan

*Corresponding author:

Dr. Satoshi Yamaguchi

Department of Biomaterials Science, Osaka University Graduate School of Dentistry,

1-8 Yamadaoka, Suita, Osaka 565-0871, Japan

Email: yamagu@dent.osaka-u.ac.jp

Tel/Fax: +81-6-6879-2919

Abstract

Background: We sought to evaluate a new regional segmentation method for use with three-dimensional (3D) non-contrast abdominal CT images and to report the preliminary results.

Methods: The proposed method was evaluated in ten cases. Manually segmented areas were used as the gold standard for evaluation. To compare the standard and the extracted liver regions, the degree of coincidence *R*% was redefined by transforming a volumetric overlap error. We also evaluated the influence of varying the density window size in terms of setting the starting points.

Results: We confirmed in ten cases that our method could segment the liver region more precisely than the conventional method. A size of window 15 voxels was optimal as the starting point in all cases.

Conclusions: We demonstrated the accuracy of a 3D semiautomatic liver segmentation method for non-contrast CT. This method promises to offer radiologists a time-efficient segmentation aid.

Keywords: Liver/AH; Computed Tomography; Probabilistic Models; Region-growing methodology

Introduction

Medical imaging modalities such as computed tomography (CT), positron emission tomography (PET), single photon emission computed tomography (SPECT), and magnetic resonance imaging (MRI) are often used to image the human body in three dimensions (3D) and to detect malignant tumors at an early stage. However, the large number of images generated during a single examination may complicate interpretation. Various computer-aided diagnostic (CAD) systems have been developed and applied to clinical cases to reduce such issues [1–8]. Because of its complex surgical anatomy, localization of liver lesions to the involved segment or segments is important. With an increasing number of liver cancer patients [9, 10], segmentation methodology is receiving critical attention [11–13].

Several studies have reported that multiple phase imaging is useful for improving automatic segmentation accuracy [11]. A level-set method that recognizes tumors by using rough segmentation results [12, 13] and a graph cuts-based [14] method for interactive regional segmentation that selects an object and background as a seed [15] have also been proposed.

The appearance of non-contrast CT images is markedly different from those of contrast CT images in terms of boundaries with other organs. Liver segmentation on non-contrast CT images has been achieved by using a conditional statistical shape model. However, this method still encounters difficulties when the morphology of the liver is abnormal [16].

We have evaluated a new segmentation method for use with non-contrast abdominal CT images. This new method promises to reduce the computational cost for detection of diseases such as hepatocellular carcinoma in the CAD systems because it can exclude other organs from the targeted liver region.

Considerable closeness to adjacent organs can be seen with a non-contrast segmentation method. A probabilistic abdominal atlas that provides human anatomical information has been developed [17, 18]. These segmentation methods for multiple organs are clearly beneficial [17]; however, the problem of low accuracy for segmentation regarding the boundaries remains. The results of manually set landmarks were different from those obtained when the landmarks for registration were set automatically [17].

We focused on the advantages of the region-growing method and the probabilistic atlas that make it possible to segment liver regions even if the liver shape and size are abnormal, owing to disease or surgery. We herein propose a new 3D regional segmentation method for use with non-contrast abdominal CT images. We also evaluated its capability in ten cases and report the preliminary results.

Materials and Methods

2.1. Extraction of a liver candidate region by the region-growing method

Figure 1 is a flow chart of the proposed method. A median filter (3 × 3 × 3) is applied to CT images to reduce noise. A conventional region-growing method is employed to extract a rough picture of the liver [19]. With this method, it is possible to select false starting points, such as blood vessels inside the liver region, even in normal liver. To solve this problem, precise region segmentation was accomplished by devising a method to select correct starting points using the following procedures.

Step 1. A user manually determines the position of window $w \times w \times w$ in a liver region and a histogram of CT values in this region is created automatically. In a clinical situation, the radiologist would empirically place this region of interest (ROI) to exclude blood vessels. As a starting point, the voxel in the ROI whose intensity has the maximum frequency in the histogram is selected automatically.

Step 2. If the CT value of each of the six voxels adjacent to the first voxel satisfies conditions 1 and 2, below, those voxels are set as new starting points.

Condition 1: $|V - V_S| < \alpha$

Condition 2: $|V - V_{N_i}| < \beta (i = 1 \cdots 6)$,

where V is the CT value of the voxel in question, V_s is the CT value that was determined to be the starting point in step 1, V_{Ni} is the CT value of the six adjacent voxels, and α and β are thresholds.

Step 3. The starting points after step 2 are set as one of the candidate liver regions and are removed as previous starting points.

Step 4. Steps 2 and 3 are repeated until all starting points are removed. The region-growing method is stopped at this time.

2.2. Construction of a correlation map

A correlation map is constructed by calculating the correlation coefficients of the locoregional histogram between the window that the starting point was located at the center of gravity and the other window, once for each voxel in step 1. Here, the window is slightly different compared with the initial window in terms of the starting point located at the center of gravity. The initial window is manually generated by radiologists

and other windows are automatically generated.

A histogram H_1(j) (j = min to max) is constructed to determine the window size $w \times w \times w$ based on the starting point and m_1. Here, j is the CT value, H_1(j) represents the number of voxels for its CT value, and m_1 represents the average number of voxels with each CT value within the window. The maximum and minimum CT values for all CT images are represented as *max* and *min*, respectively.

Next, a histogram H_2 (j) is constructed based on each voxel, as is the case in H_1 (j). The average number of voxels for each CT value within the window is m_2. Correlation coefficients *C(i)(i* = 1-*voxel size)* are calculated by Eq. (1), where *voxel size* is the number of voxels for all CT images.

$$C(i) = \frac{\sum_{j=\min}^{\max} (H_1(j) - m_1)(H_2(j) - m_2)}{\sqrt{\sum_{j=\min}^{\max} (H_1(j) - m_1)^2} \sqrt{\sum_{j=\min}^{\max} (H_2(j) - m_2)^2}} \qquad (1)$$

Only positive correlation coefficients 0–1 are used. Minus values are replaced with 0 since the negative correlations indicate an inverted region of the window. An obtained correlation coefficient is set as the value of each voxel, and the results were applied to the liver candidate region *C(i)*.

2.3. Construction of the probabilistic atlas

A probabilistic atlas was constructed by other cases compare with the correlation map. Liver regions were manually segmented from all cases and three-dimensional rigid transformation was performed by open source software (Insight Segmentation and Registration Toolkit; Kitware Inc., Clifton Park, NY, USA). CT values in the liver region for each transformed volume were replaced to 1 (white) as a maximum value of the probability that is liver region. Other regions were set as 0 (black). All volumes were overlaid. Then, average values (0 to 1) once every voxels were calculated. In this study, we used this volume as the probabilistic atlas.

2.4. Registration between the targeted CT images and the probabilistic atlas

Thin-plate spline (TPS) [20] was used to perform registration between the targeted CT images and the probabilistic atlas, in terms of size and shape. The required landmarks for registration were selected by an operator: the hepatic portal, lateral tip of the left hepatic lobe, inferior margin of the right hepatic lobe, because of their anatomical specifications using volume-rendering software (VolView; Kitware).

Although there was 3D visualization in the volume-rendering software, 30 positions in the 3D coordinate system were manually recorded by a mouse-pointing operation. To avoid the risk of selecting another region, the probabilistic atlas was visualized for only regions of probability = 1. Additionally, the correlation coefficient in section 2.4 had the possibility of false recognition that adjacent liver tissue was not a liver region because of low correlation coefficients around the liver boundary. Thus, landmarks were located on the surface of the probabilistic atlas (probability = 1) and matched to the liver surface on CT images.

Figure 2 shows examples of the locations of the adopted landmarks, where each landmark is represented by a red point. Figure 2 shows the probabilistic atlas of the input data sets. The probabilistic atlas has a distribution within 0–1: the whiter the region, the higher the probability of it being a liver region. In all cases, regions of probability = 1 correspond to liver regions that were used to generate the probabilistic atlas.

2.5. Segmentation by maximization of posterior probability

Liver region segmentation was performed by using the probabilistic atlas after registration mentioned in section 2.4. The maximum posterior probability between the targeted data and the probabilistic atlas was used to extract liver region. Posterior probability was calculated by Bayes' theorem following Eq. (2), and one organ label with the maximum posterior probability for each pixel was allocated as liver region [18].

$$P(n|v) = \frac{p(v|n)P\{n\}}{p(v)} \quad (2)$$

$$p(v) = \sum_{n=1}^{N} p(v|n)P\{n\} \quad (3)$$

,

where n is the organ label, v is the CT value, $p(v/n)$ is the probability density function of the CT value v related to organ n, $P\{n\}$ is the prior probability (the value of the probabilistic atlas), and N is the number of organs labeled. In this study, the organs labeled in the liver region and the background were selected as 1 and 2, respectively.

2.6. Extraction of the liver candidate region using the correlation map and probabilistic atlas

After maximizing the posterior probability, the liver candidate region was

segmented using the probabilistic atlas and the correlation map. To create the condition whereby both the probabilistic atlas and the correlation map $C(i)$ of the targeted voxel had high values, the liver candidate region $L(i)$ that was over threshold t was extracted following Eq. (4):

$$L(i) = \begin{cases} TRUE & if \quad A(i) \times C(i) > t \\ & \quad (i = 1,2,3, \cdots, voxel\ size) \\ FALSE & else \end{cases} \qquad (4)$$

,

where threshold t was determined by the relation and the average μ and standard deviation σ of $A(i) \times C(i)$. *Voxel size* indicates the number of all voxels for $A(i)$ or $C(i)$. Threshold t was determined automatically by selecting a data range of $\mu \pm 3\sigma$, obtaining the left term of Eq. (4). Additionally, 99.73 % of the data in the histogram were selected as the liver candidate region.

2.7. Liver region extraction by morphology processing

The liver candidate region has blood vessels and noise depending on the CT parameters such as tube current, voltage, and slice thickness. Therefore, morphological processing was performed. After a dilation process (described below), an erosion

process was applied the same number of times as the dilation process for a specific region of high value in the probabilistic atlas and in the liver candidate region for filling a region of blood vessels. Six neighbor voxels of the targeted voxel were replaced from 0 (black) to 1 (white) when a white voxel in six neighbor voxels existed in at least one. This process was called the dilation. The opposite process was called the erosion.

2.8 Experiments

The method was applied to 3D non-contrast abdominal CT images from ten cases provided by the Japanese Society of Medical Imaging Technology. The CT scans included both healthy livers and livers with hepatocellular carcinoma, as shown in Table 1. A probabilistic atlas was constructed from cases that were different from those of the ten study cases. The specifications of nine CT data sets were 512 × 512 pixels, 26 slices, 0.63 × 0.63 mm pixel spacing, and 7.00 mm slice thickness. These images were of healthy cases. All CT images were acquired using a four-slice scanner (Aquilion 4DAS®, Toshiba Medical Systems Corporation, Tochigi, Japan). To combine the correlation map and the probabilistic atlas, linear interpolation and isotropic processing

1 was performed because the abdominal images and the probabilistic atlas had different
2 resolutions for longitudinal and orthogonal directions.
3 A 15 × 15 × 15 voxels window was used as the threshold in step 1, thresholds α
4 = 10 and ß = 5 were used in step 2, and the probability for the erosion process was set at
5 >0.8. Table 2 shows the threshold *t* in Eq. (4) and the number of dilations and erosions
6 for the morphology process. The number of morphology process was determined
7 empirically.
8 We assumed that clinicians do not assign a window that includes the inferior
9 vena cava or portal vein; Thresholds in step 2 were α = 10 and β = 5, and window sizes
10 were 5, 10, and 15 voxels. We then calculated the ratios of the areas with a blood vessel
11 included in the liver region for each window and developed a histogram with a
12 longitudinal axis of the number of pixels versus the ratio for each of the ten cases. For
13 the development of the histogram, the blood vessel regions were segmented from an
14 early-arterial and a portal-venous phase for each of the ten cases. Two types of
15 segmented blood vessel region were overlaid and volume contents for three-types of the
16 window were calculated.

Lastly, we evaluated the accuracy for the final liver region. The manually segmented area was used as the correct area for evaluation. To compare the correct region and the extracted liver region, the degree of coincidence R% was redefined by transforming a volumetric overlap error [21] as follows:

$$R = \frac{n(N_R \cap N_S)}{n(N_R \cup N_S)} \times 100, \qquad (5)$$

where the correct liver region is N_R, a region extracted by the proposed method is N_S, and the number of pixels within the area Z is $n(Z)$.

We evaluated the influence of varying the window size in terms of setting the starting points in Step 1.

Results

Figure 3 shows the extracted results for each process using case 6 as an example. The area enclosed by the red line represents the liver region. The semitransparent red area indicates the segmented region. The red rectangle was drawn to represents the region in the case of a 15 × 15 × 15 voxels window. The area in the green ellipse represents the spleen. As shown in Fig. 3(b), the segmented area derived using the region-growing method includes the spleen, not just the liver. The accuracy of the segmented region derived by the probabilistic atlas was low, as shown in Fig. 3(c).

By calculating the correlation coefficient between an adjacent area around the starting point and another area, the boundary of the liver could be segmented, as shown in Fig. 3(d), whereas the probabilistic atlas could not segment it correctly (Figs. 3[b, c]). Additionally, we confirmed that the area of the spleen enclosed in the green line was removed correctly using the probabilistic atlas (Fig. 3[b]). Figure 4 shows a variation of the correlation map and the probabilistic atlas in each region for case 6. Part of the area enclosed in the red line in Fig. 4 includes the liver region.

Part of the area enclosed by the green ellipse, shown in Fig. 4(c), is the area in

which the spleen had been. In each image, as the red area increases, the value becomes higher, with a larger blue area indicating a low value. Figure 4(a) shows that the correlation coefficient of the liver region is high and that of the other region is low. In addition, the value of the probabilistic atlas decreases around the liver boundary in the area near the spleen, as seen in Fig. 4(b). Figure 4(c) shows that by combining the variation of the correlation coefficient and the probabilistic atlas, the liver boundary in the area near the spleen can be segmented. The other cases showed a similar tendency. Figure 5 shows the number of voxels for the content ratio of the vessel area for different window sizes. In the case of a size 15 voxel window, there were numerous pixels with few ratios for including the area of blood vessels. In contrast, with window sizes 5 and 10 the ratios were about 1–10%.

Table 3 shows the results of the accuracy of the evaluation of each case. Figure 6 shows the results of case 5, with segmentation performed using the proposed method. The portion of the area enclosed in the red line in Fig. 6 is the liver region, and the semitransparent red region is the segmented region.

Discussion

Using 3D locoregional histograms, we were able to calculate the correlation coefficient between a single voxel in the liver region and that in another region. Specifically, the correlation coefficients at the boundary between the liver and other organs were different from those inside the liver region.

In terms of segmentation accuracy, the proposed method gave us better results than the region-growing method alone or the probabilistic atlas alone (Table 3). At this stage, the proposed method has the potential to overcome the limitation relating with the unclear boundary of the probabilistic atlas, even if the probabilistic atlas was constructed with few CT images. The liver boundary was segmented accurately by the region-growing method. Over-segmentation related to the spleen and heart was avoided by applying the probabilistic atlas. Additionally, the degree of coincidence in a liver candidate region that was segmented by Eq. (4) in cases 1, 4, and 9 showed low segmentation accuracy when compared with that using the region-growing method. These differences resulted from the area being eliminated by the thresholding process because of a low correlation coefficient near blood vessels in the liver and liver

boundary.

We considered a case in which the area of the size 5 window passed through the area that included blood vessels. It is possible that windows of sizes 5 and 10 voxels compared to 15 voxel have a lower CT value than those of the liver region at the starting point, influencing the CT value in the area of blood vessels. A size 15 window was selected because the CT value of the liver region was chosen as the starting point in all cases.

A nonsegmented liver region was noted even when using the proposed method (Fig. 6). This finding may have been the reason that precise segmentation of the liver candidate region could not be accomplished (see section 2.2), because there were specific areas in the liver where the CT values were markedly low. Additionally, the liver candidate region that was selected (see section 2.2) had an adjacent muscle and fatty area with a CT value similar to that of the liver region and an over-segmented region excluding the liver region. In the case of non-segmentation of the liver candidate region with inaccuracy (see section 2.2), the liver boundary often became fuzzy because the correct liver region was blocked by an over-segmented region near the liver

boundary that excluded the liver region. Additionally, in the case of registration (described in section 2.4), it was difficult to recognize the liver boundary visually and place landmarks correctly even manually. Although the operators required much time (>30 minutes) for placing the landmarks, total time spent on the whole segmentation procedure was usually less than 1 hour even if other automated segmentation times were included.

For this reason, improving the extraction accuracy was difficult. As shown in Table 3, identifying the segmented liver region by the proposed method confirmed its improved accuracy of the proposed method when its results were compared with results for the segmented liver region obtained by the probabilistic atlas.

Other organs or tissues were still extracted when the CT values were similar to those of liver. One solutions is to devise a way to improve the accuracy of segmentation of the liver boundary. Implementation of an automatic landmarking function for registration is ongoing to reduce the computational time.

Conclusions

By generating a correlation map from correlation coefficients between an area adjacent to the starting point and another area, we successfully demonstrated 3D liver segmentation. After comparing the results of the conventional method, we found that our method offered better results. We effectively confirmed the advantages of our method by applying it to ten cases. Within the limitations of semi-automatic liver segmentation, our proposed method has a great potential to offer radiologists more time efficiency.

Acknowledgments

This work was supported by Grants-in-Aid for Scientific Research Nos. 21240017 and 24592955 from the Japan Society for the Promotion of Science, Japan.

References

1. Shiraishi J, Li Q, Appelbaum D, Doi K. Computer-aided diagnosis and artificial intelligence in clinical imaging. *Semin Nucl Med* **41** (2011) 449-462.

2. Chen H, Xu Y, Ma Y, Ma B. Neural network ensemble-based computer-aided diagnosis for differentiation of lung nodules on CT images: clinical evaluation. *Acad Radiol* **17** (2010) 595-602.

3. Alomari RS, Corso JJ, Chaudhary V, Dhillon G. Computer-aided diagnosis of lumbar disc pathology from clinical lower spine MRI. *Int J Comput Assist Radiol Surg* **5** (2010) 287-293.

4. Kiszka K, Haduch J, Pasowicz M. Application of computer aided diagnosis (CAD) in clinical imaging. Presentation of the value and current directions in CAD development in various imaging techniques based on literature review. *Przegl Lek* **66** (2009) 437-447.

5. Li H, Giger ML, Yuan Y, Chen W, Horsch K, Lan L, et al. Evaluation of computer-aided diagnosis on a large clinical full-field digital mammographic dataset. *Acad Radiol* **15** (2008) 1437-1445.

6. Goggin LS, Eikelboom RH, Atlas MD. Clinical decision support systems and computer-aided diagnosis in otology. *Otolaryngol Head Neck Surg* **136** (2007) S21-26.

7. Buhmann S, Herzog P, Liang J, Wolf M, Salganicoff M, Kirchhoff C, et al. Clinical evaluation of a computer-aided diagnosis (CAD) prototype for the detection of pulmonary embolism. *Acad Radiol* **14** (2007) 651-658.

8. Wormanns D, Fiebich M, Saidi M, Diederich S, Heindel W. Automatic detection of pulmonary nodules at spiral CT: clinical application of a computer-aided diagnosis system. *Eur Radiol* **12** (2002) 1052-1057.

9. El-Serag HB, Davila JA, Petersen NJ, McGlynn KA. The continuing increase in the incidence of hepatocellular carcinoma in the United States: an update. *Ann Intern Med* **139** (2003) 817-823.

10. Gottlieb S. US reports increase in liver cancer. *BMJ* **318** (1999) 755A.

11. Rusko L, Bekes G, Fidrich M. Automatic segmentation of the liver from multi- and single-phase contrast-enhanced CT images. *Med Image Anal* **13** (2009) 871-882.

12. Smeets D, Loeckx D, Stijnen B, De Dobbelaer B, Vandermeulen D, Suetens P.

Semi-automatic level set segmentation of liver tumors combining a spiral-scanning technique with supervised fuzzy pixel classification. *Med Image Anal* **14** (2010) 13-20.

13. Lee J, Kim N, Lee H, Seo JB, Won HJ, Shin YM, et al. Efficient liver segmentation using a level-set method with optimal detection of the initial liver boundary from level-set speed images. *Comput Methods Programs Biomed* **88** (2007) 26-38.

14. Boykov Y, Funka-Lea G. Graph cuts and efficient N-D image segmentation. *Int J Comput Vision* **70** (2006) 109-131.

15. Chen Y, Wang Z, Hu J, Zhao W, Wu Q. The domain knowledge based graph-cut model for liver CT segmentation. *Biomed Signal Process Control* **7** (2012) 591-598.

16. Tomoshige S, Oost E, Shimizu A, Watanabe H, Nawano S. A conditional statistical shape model with integrated error estimation of the conditions; Application to liver segmentation in non-contrast CT images. Med Image Anal **18** (2014) 130-143.

17. Park H, Bland PH, Meyer CR. Construction of an abdominal Probabilistic atlas and its application in segmentation. *IEEE Trans Med Imaging* **22** (2003) 483-492.

18. Okada T, Shimada R, Hori M, Nakamoto M, Chen YW, Nakamura H, et al. Automated segmentation of the liver from 3D CT images using probabilistic atlas and multilevel statistical shape model. *Acad Radiol* **15** (2008) 1390-1403.

19. Sandor T, Metcalf D, Kim YJ. Segmentation of brain CT images using the concept of region growing. *Int J Biomed Comput* **29** (1991) 133-147.

20. Bookstein FL. Principal warps - thin-plate splines and the decomposition of deformations. *IEEE Trans Pattern Anal* **11** (1989) 567-585.

21. Heimann T, van Ginneken B, Styner MA, Arzhaeva Y, Aurich V, Bauer C, et al. Comparison and evaluation of methods for liver segmentation from CT datasets. *IEEE Trans Med Imaging* **28** (2009) 1251-1265.

Summary

Medical imaging modalities such as computed tomography (CT), positron emission tomography, single photon emission computed tomography (SPECT), and magnetic resonance imaging are often used for scanning the human body in three dimensions. With their wide range of capabilities and high resolution, they can detect malignant tumors at an early stage. The large number of images obtained at a single session may confuse their interpretation and become a great burden in terms of time-consuming tasks for the radiologist. Various computer-aided diagnostic (CAD) systems have been developed and applied to clinical cases to reduce such burdens. In CAD systems, once the region or organ suspected of disease is identified, its segmentation is crucial to determine the precise diagnosis. With an increasing number of liver cancer patients, segmentation is becoming a focus for diagnostic purposes.

We focused on the advantages of the region-growing method and the probabilistic atlas that make it possible to segment the liver even if its shape and size are varied depending on individual differences in each clinical case and to prevent misssegmentation for multiple organs, respectively. We herein propose a new regional

segmentation method for use with three-dimensional (3D) non-contrast abdominal CT images. We also evaluated its capability in ten cases and report the preliminary results.

The proposed method was applied to 3D non-contrast abdominal CT images from ten cases. Additionally, a probabilistic atlas was developed using nine liver region data sets by normalizing the position and orientation through rigid transformation. We evaluated the accuracy for the final liver region. The manually segmented area was used as the correct area for evaluation. To compare the correct region and the extracted liver region, the degree of coincidence *R*% was redefined by transforming a volumetric overlap error. Additionally, we evaluated the influence of varying the window size in terms of setting the starting points.

We confirmed in ten cases that our method could segment the liver region more precisely than the conventional method. A size of window 15 voxel was selected because the CT value of the liver was chosen as the starting point in all cases.

We proposed a liver segmentation method using 3D non-contrast abdominal CT images. By generating a correlation map from correlation coefficients between an area adjacent to the starting point and another area, we successfully demonstrated 3D liver

segmentation. After comparing the results of the proposed method with those obtained with the region-growing method and the probabilistic atlas, we found that our method offered better results. We effectively confirmed the advantages of the proposed method by applying it to ten cases. Within the limitations of semi-automatic liver segmentation, our method promises to offer radiologists a time-efficient segmentation aid.

Tables

Table 1 Specification of CT dataset used

No.	Disease	Sex	Age	Slice-thickness (mm)	Pixel-spacing (mm)	Number of slices
1	HCC	Female	56	2.0	0.549	158
2		Male	71	2.0	0.625	177
3	HCC	Male	54	2.0	0.625	185
4		Male	65	2.0	0.625	154
5	HCC	Male	65	2.0	0.625	186
6	HCC	Female	77	2.0	0.546	181
7	HCC	Male	41	2.0	0.625	176
8	HCC	Male	67	2.0	0.625	166
9	HCC	Male	64	2.0	0.625	185
10	HCC	Male	69	2.0	0.586	166

Table 2 Threshold *t* and the number of erosion and dilation (opening) processes

Case	Threshold	Erosion	Dilation
1	0.70	4	4
2	0.70	4	4
3	0.70	4	4
4	0.63	3	3
5	0.72	6	6
6	0.70	4	4
7	0.71	3	3
8	0.71	3	3
9	0.70	3	3
10	0.71	4	4

Table 3 Degree of coincidence (%)

RG: region-growing method; PA: probabilistic atlas; CR: candidate region; PM: proposed method

Case	RG	PA	CR	PM
1	88.71	71.71	83.66	89.02
2	83.17	70.64	83.73	89.58
3	83.32	69.79	84.83	92.03
4	93.06	72.89	88.39	93.69
5	48.36	66.51	68.75	75.51
6	81.32	74.19	85.01	91.31
7	69.68	68.80	82.03	88.12
8	68.25	68.26	83.74	91.58
9	87.57	67.29	87.17	90.70
10	61.82	72.67	78.08	86.00

1 **Figures**

2

3 Figure 1

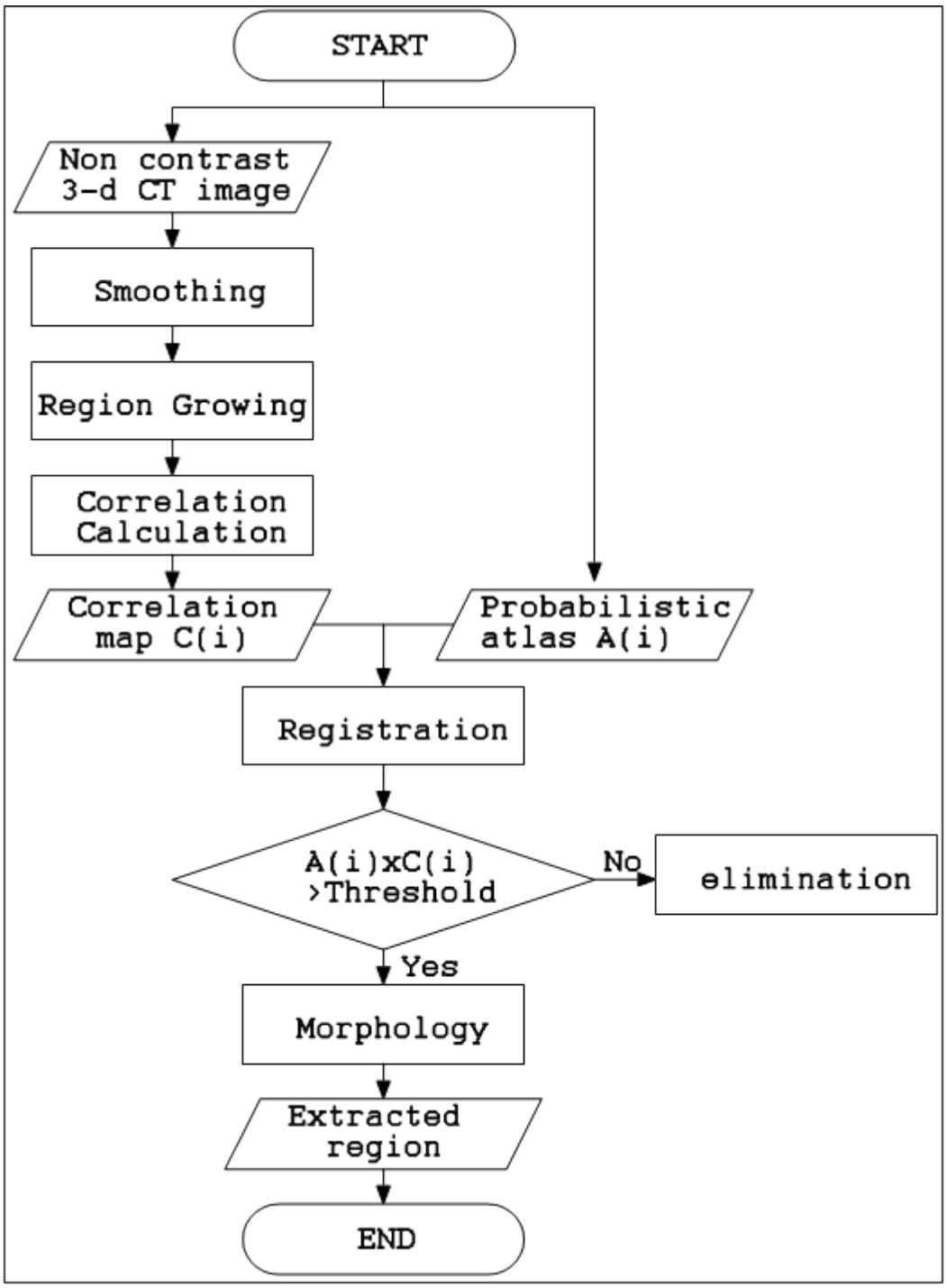

4

Figure 2

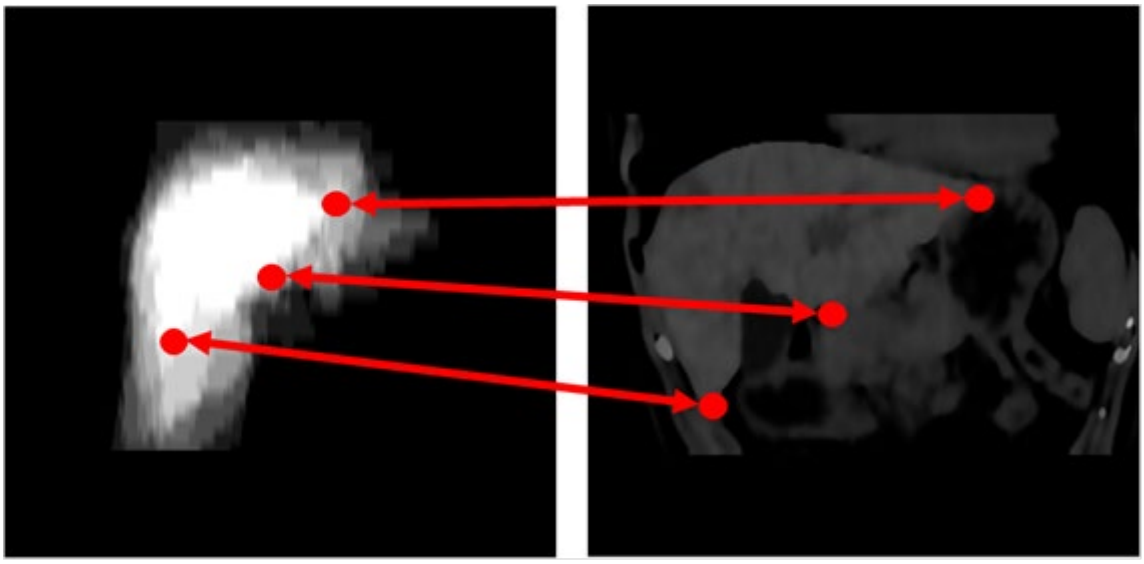

Figure 3a

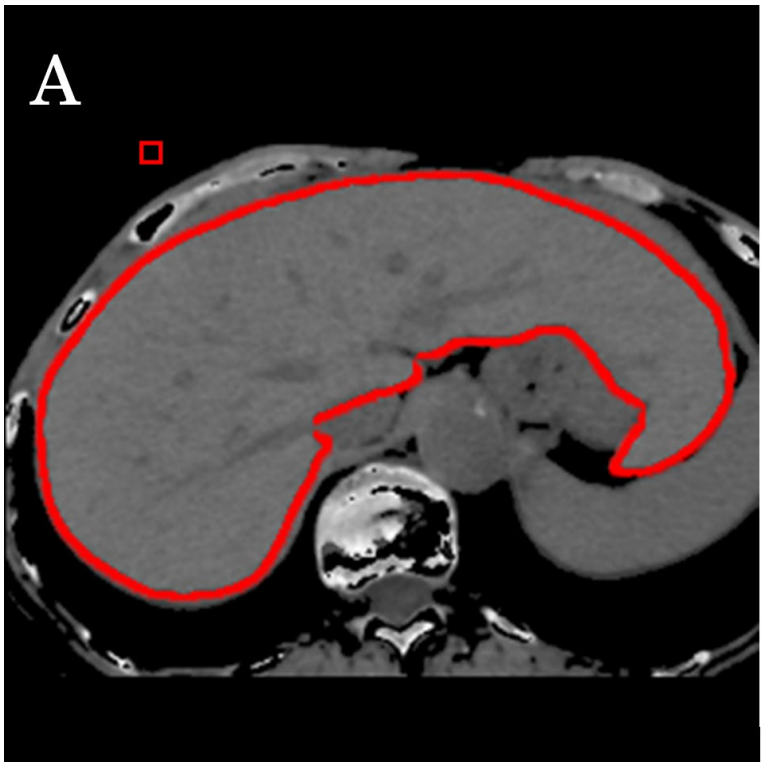

Figure 3B

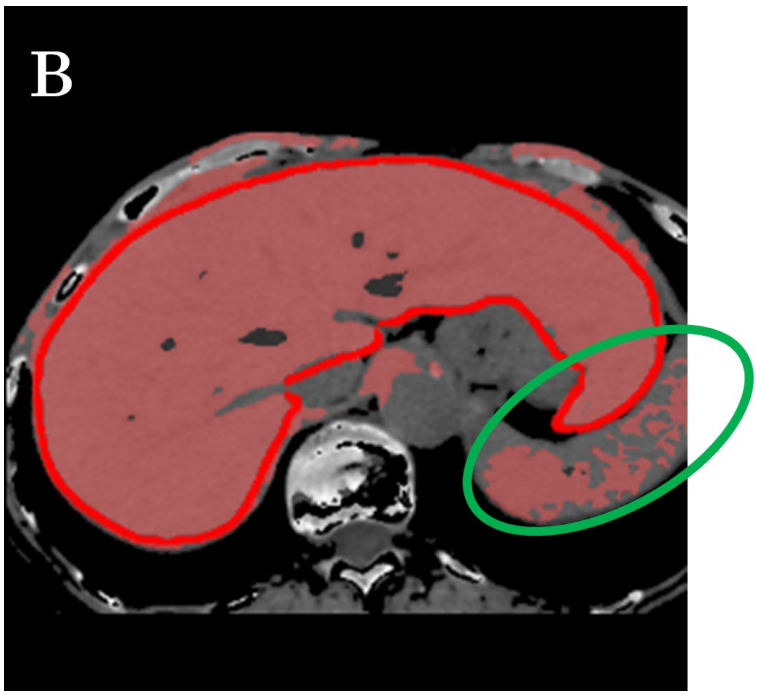

Figure 3C

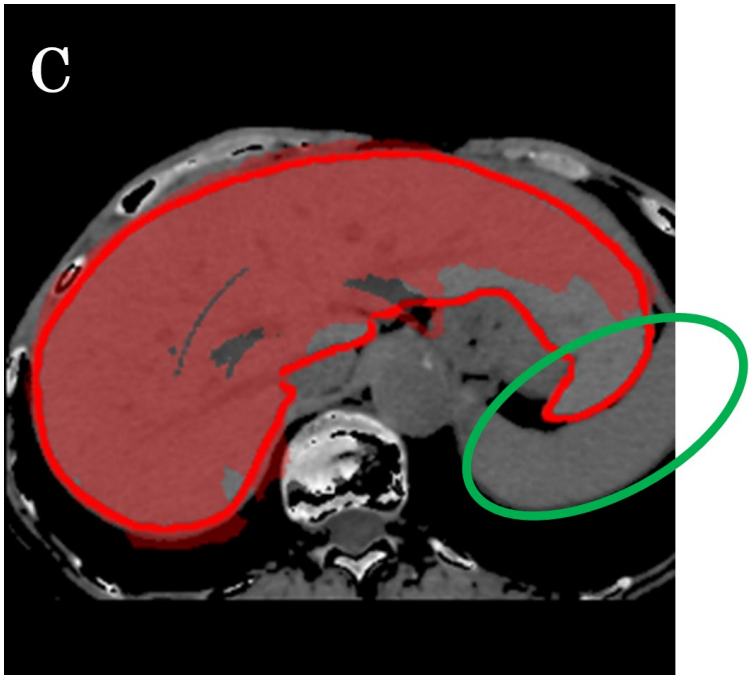

Figure 3D

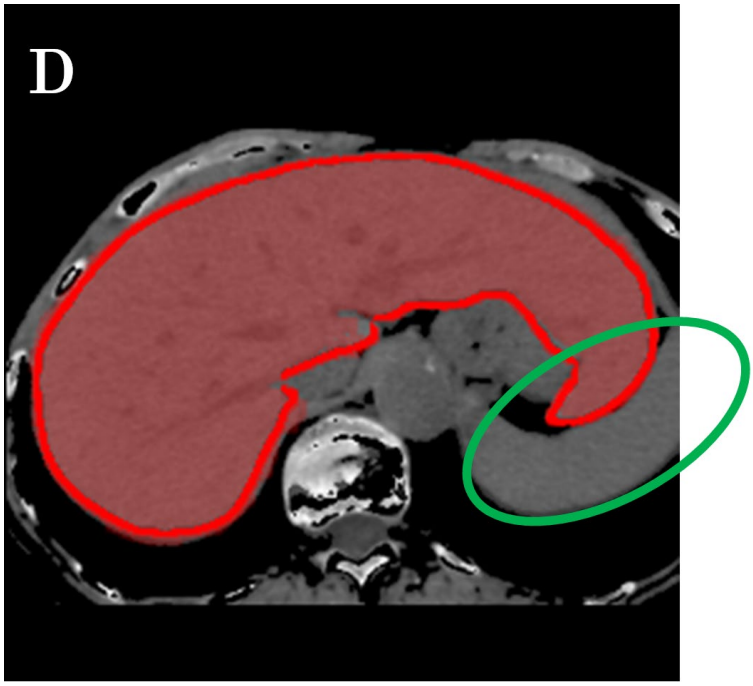

Figure 4A

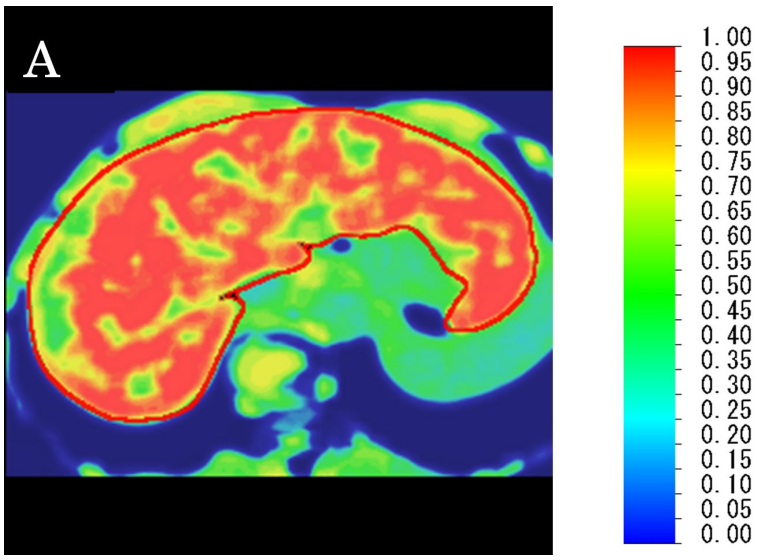
A
1.00
0.95
0.90
0.85
0.80
0.75
0.70
0.65
0.60
0.55
0.50
0.45
0.40
0.35
0.30
0.25
0.20
0.15
0.10
0.05
0.00

Figure 4B

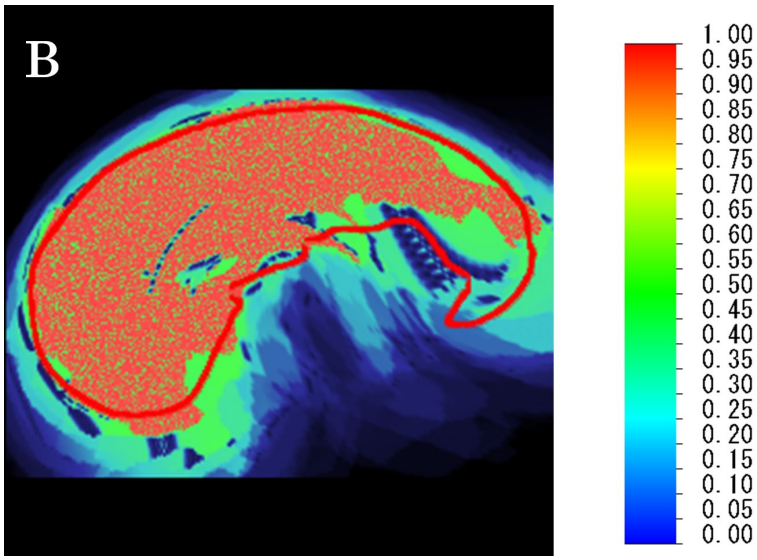
B
1.00
0.95
0.90
0.85
0.80
0.75
0.70
0.65
0.60
0.55
0.50
0.45
0.40
0.35
0.30
0.25
0.20
0.15
0.10
0.05
0.00

Figure 4C

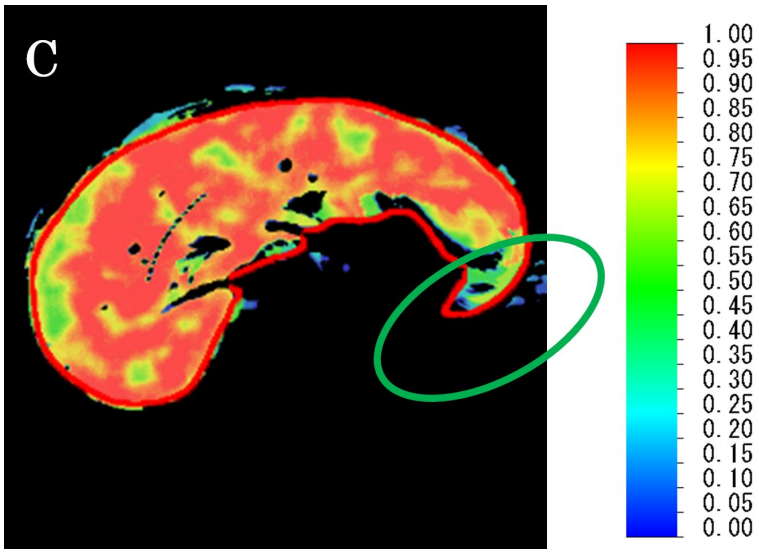
C
1.00
0.95
0.90
0.85
0.80
0.75
0.70
0.65
0.60
0.55
0.50
0.45
0.40
0.35
0.30
0.25
0.20
0.15
0.10
0.05
0.00

1 Figure 5

2

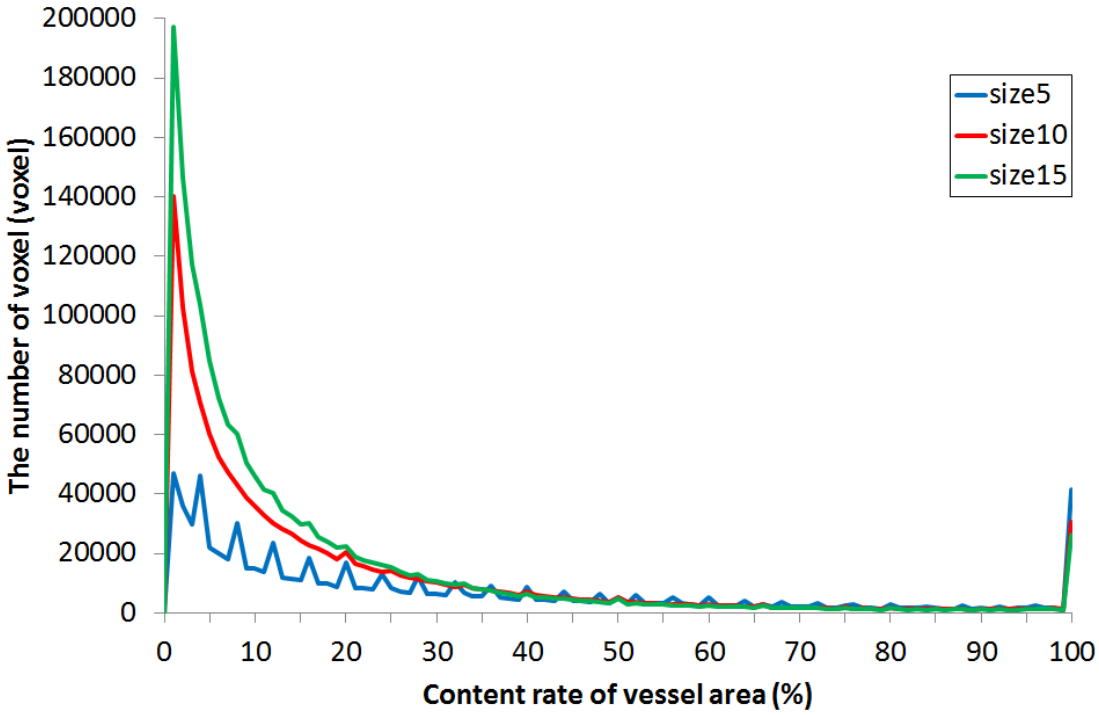

3

4

Figure 6A

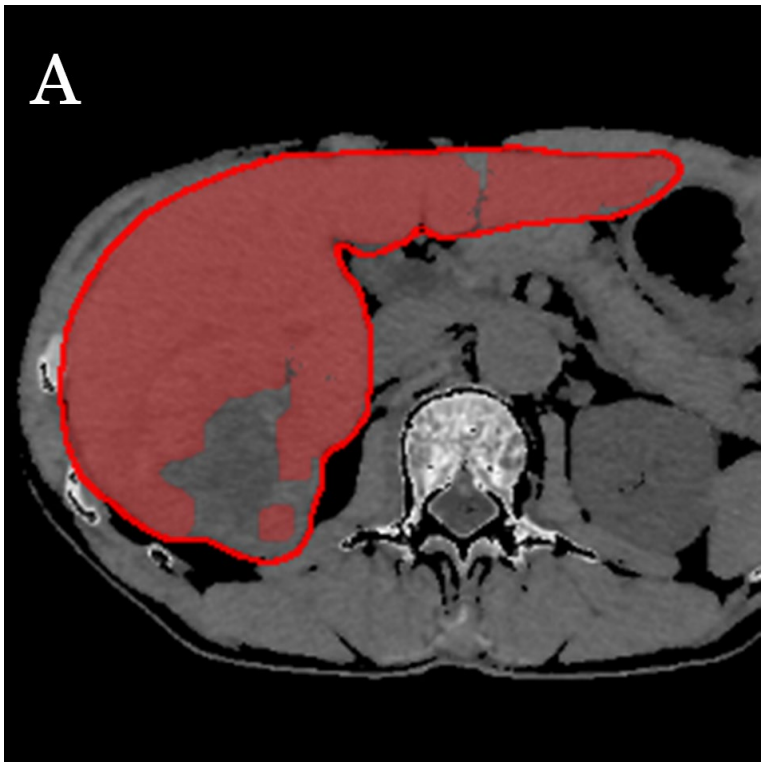

Figure 6B

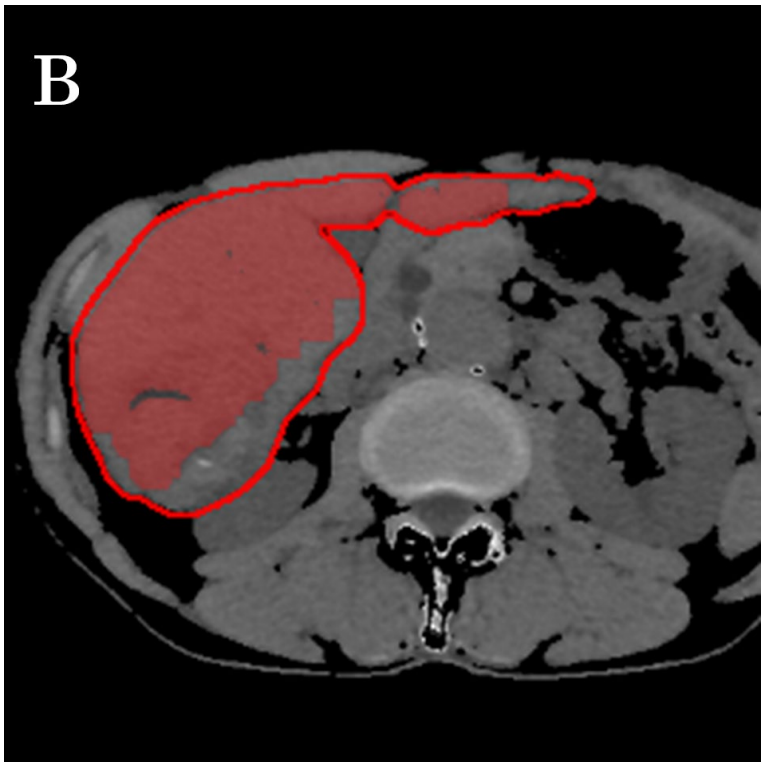

Figure Legends

Fig. 1 Flow chart of proposed three-dimensional liver segmentation for non-contrast computed tomography images.

Fig. 2 Examples of positioning of landmarks. Left: probabilistic atlas. Right: input data of case No.1. Red points represent landmarks of the inferior tip of the right lobe of the liver (left lower image), the hepatic portal (middle image), and the lateral tip of the left lobe of liver (right upper image).

Fig. 3 Extracted region of case No.6 derived by each process. (A) Input data. (B) Segmented region determined by region-growing method. (C) Segmented region determined by probabilistic atlas, with probability >0.95 after registration. (D) Segmented region determined by proposed method. Red and green lines represent the liver and spleen region, respectively. Translucent red areas represent segmented region by each method.

Fig. 4 Distribution with each process. (A) Correlation map. (B) Probabilistic atlas. (C) $A(i) \times C(i)$of the segmented region (see section 2.6). Color bars represent the values of the correlation coefficient, existence probability of liver, and product of existence probability of liver and correlation coefficient.

Fig. 5 The number of voxels once every volume contents of vessel area for sizes of window 5, 10, and 15 voxels.

Fig. 6 Example of failures in case 5. (A) Slice number 78. (B) Slice number 94.